AIAA SciTech Forum
4-8 January 2016, San Diego, California, USA
54th AIAA Aerospace Sciences Meeting

10.2514/6.2016-1053

X-56A Aeroelastic Flight Test Predictions

Daniel A. Reasor Jr.,*
Air Force Research Laboratory – Eglin AFB, FL 32542
Keerti K. Bhamidipati†
Air Force Test Center – Edwards AFB, CA 93524
Alexander W. Chin‡
NASA Armstrong Flight Research Center – Edwards AFB, CA 93523

The unstructured fixed wing flow solver CREATE™-AV Kestrel was used to perform high-fidelity aeroelastic simulations of the X-56A aircraft undergoing maneuvers, representative of flight test. Validation of the predicted aerodynamic performance characteristics are performed through comparison of force and moment coefficients with ground and flight test results. All grids were constructed using CREATE™-MG Capstone. Aeroelastic validation will be performed by assessing loads, accelerometer data, leading edge stagnation point, and body-freedom flutter onset speed from future NASA Armstrong flight tests.

Nomenclature

A	=	wing area, in^2	α	=	angle-of-attack, deg
b	=	wing span, in	β	=	angle-of-sideslip, deg
c	=	wing chord, in	$\delta_{99\%}$	=	estimated boundary layer height, in
C_p	=	pressure coefficient	δ_H	=	total viscous grid height, in
D	=	drag force, lb	ΔMa_∞	=	freestream Mach number increment
GCI	=	grid convergence index	Δs_1	=	initial wall-normal grid spacing, in
GF	=	geometric growth factor	$\Delta s_{\text{surface}}$	=	max surface grid spacing, in
L	=	lift force, lb	Δs_{LE}	=	leading edge grid spacing, in
$\mathbf{L}_M$	=	moment lengths, in	Δt	=	time step, sec
m_n	=	generalized modal mass of mode n	ν	=	kinematic viscosity, in^2/sec
$m_n^{\text{eff}}(t)$	=	modal effective mass of mode n	ρ	=	density, snails/in^3 (slug·ft/in^4)
Ma_∞	=	Mach number	τ	=	non-dimensional timescale, tf_{S1WB}
p	=	pressure, lb/in^2			
q	=	dynamic pressure, lb/in^2			
r	=	grid refinement factor			
Re	=	Reynolds number			
$\omega_n(t)$	=	modal weight of mode n			
W	=	weight, lb			
y^+	=	inner scaling for wall-normal direction			
$\mathbf{x}$	=	reference coordinate, in			

*Munitions Aerodynamics Sciences Branch, Senior AIAA Member
†412th Test Engineering Group, AIAA Member
‡Aerostructures Branch, Senior AIAA Member; Ph.D. Student, University of Washington

I. Introduction

ACCOMODATING future requirements of increased endurance and range for transport aircraft require high lift over drag (L/D) designs and the use of light weight structures leading to several aeroelastic and aeroservoelastic challenges.[1,2] Fatigue, flutter, divergence, control reversal, and gust load alleviation are some of the phenomena that pose a challenge to lightweight designs. Instead of adding additional structural stiffness (and weight) to avoid structural failure, active aeroelastic control is an attractive alternative approach for future lightweight aircraft. The benefits of this technology include increased control power, reduced aerodynamic drag, reduced maneuver loads, and reduced structure and takeoff weights while permitting aircraft designs with thinner wings and larger wingspans.[3]

The X-56A Multi-Utility Technology Testbed (MUTT) program is focused on active flutter suppression technology and active shape control. Recent efforts at NASA Armstrong use the X-56A as a test bed for the testing and design of sensors and controllers related to active aeroelastic control. Topics of research include: the stability of closed-loop flutter wing models where modal coordinates are obtained with fiber optics;[4] robustness with fiber optic sensor failures;[5] stabilizing and controlling wing shape;[6] fly-by-feel sensing and control;[7] and airframe structural optimization.[8,9] All of these research topics rely on an accurate structural model of the aircraft that has been verified and validated with ground vibration test (GVT) results.[10] While many of these studies make use of an accurate structural representation of the X-56A, they still employ low (panel method) to medium (Euler-like) fidelity aerodynamics. This work aims to supplement the lower-fidelity aeroelastic simulations with high fidelity Euler and viscous delayed detached eddy simulation (DDES) fluid solvers coupled with a modal structural solver.

II. Background

The X-56A is a flying wing layout which has significant potential for high cruise L/D, reduced intersection drag, and reduced wetted area.[1] The center body of the aircraft is 'rigid' while the wings are modular, i.e., multiple wing designs with different structural properties and sensor packages can be tested. More detail on the design and development of the X-56A can be found in the work by Nicolai et al.[11] and in the paper by Beranek et al.[2] The size, geometric quantities, weights, and propulsion of the X-56A are outlined in Table 1.[2] The propulsion is provided by two JetCat P400 turbine engines supplying 82 lbs (400 N) of thrust per engine. Control surfaces consist of 2 body flaps and 8 elevons (4 per wing). A weight of 495.6 lbs is used in the simulations herein.

Table 1. Dimensions and mass of X-56A configuration as simulated. Mass properties are from the NASTRAN structural model.

Description	Symbol	Value	Units
Chord Length	c	24.0	in
Wingspan	b	336.0	in
Wing Area	A	8064.0	in^2
Moment Center	$\mathbf{x}_M$	$\{165.0, 0.0, 101.3\}$	in
Moment Lengths	$\mathbf{L_M}$	$\{336.0, 24.0, 336.0\}$	in
Center of Gravity	$\mathbf{x}_{CG}$	$\{163.3, 0.2311, 101.3\}$	in
Weight	W	495.6	lbs

Lightweight, flexible aircraft must be analyzed considering interactions between the rigid-body and elastic modes as there is not sufficient separation of their respective modal frequencies.[12] The wing first bending mode frequency drops with increasing dynamic pressure (due to increased aerodynamic damping), but the aircraft short-period mode frequency increases linearly with flight speed. The short-period mode couples with the first bending wing mode, resulting in flutter at a speed lower than the static divergence speed, called body-freedom flutter.[13] For the X-56A, this is a low frequency flutter mode, on $\mathcal{O}(1)$ Hz,[10] has large center body longitudinal and outboard wing bending (wash-in) motion.

III. Setup

III.A. Solver Details

The aeroelastic solver used for this work is the CREATE^{TM}-AV product Kestrel.[14–17] Kestrel is developed for use with fixed-wing aircraft that undergo control surface deflections, six degree-of-freedom motion, maneuvers via prescribed motion, and fluid-structure interactions. All of the results presented in this work employ Kestrel version 6.1.

The unstructured flow solver within Kestrel, named KCFD, solves the compressible two- or three-dimensional Euler (inviscid), Navier–Stokes (laminar), or Reynolds-Averaged Navier–Stokes equations (turbulent) on unstructured grids using cell-centered schemes. It obtains second-order spatial accuracy by employing a weighted least squares or Green–Gauss techniques. Time marching is done in a point-implicit manner with Newton sub-iterations and is also second order accurate. The viscous simulations performed herein assume a fully turbulent flowfield and make use of the Spalart–Allmaras (SA) one-equation turbulence model[18] with the delayed detached eddy simulation methodology[19] (SA-DDES) for separated flows.

The KCFD solver employs a modified BJ limiter[20] used with the Roe inviscid fluxes, LDD+ viscous fluxes, weighted gradients, and a vanLeer convective flux Jacobian.[21,22] The Gauss–Seidel matrix scheme[23] is employed with a minimum of 8 and maximum of 64 sweeps. A global time stepping scheme is used with a time step of Δt=5.0×10^{-4} seconds using an advective temporal damping value of 0.05. Startup iterations are used to initialize each simulation with a damping ramp fraction of 0.4 with an advective damping starting value of 0.1.

The modal structural solver[17] within Kestrel solves the modal solution with a time-marching scheme that includes Newton sub-iterations and can communicate with KCFD to pass information at the sub-iteration level while maintaining second-order temporal accuracy. Mesh motion is performed using a rigid wall distance of 0.5 inches, which specifies that cells within this distance of the aircraft surface are treated as rigid elements. For the viscous aeroelastic simulations, this encompasses the entire estimated boundary layer height, but does not contain all of the prism layers. The outer limit wall distance for mesh deformation was specified as 360 inches (approximately equal to the aircraft span of 336 inches). A surface attention scaling exponent of 4.0 was specified to improve the mesh deformation in areas where surfaces intersect, e.g., the wing-winglet interface. If cells collapse during the mesh deformation process, the auto-repair mesh feature in Kestrel is employed.

III.B. Grid Generation

The grids used in this study were created with CREATE^{TM}-MG Capstone version 5.0.1 using IGS formatted computer-aided-design (CAD) geometry exported from SolidWorks 2014. Five Euler grids were generated for this effort and the details of each are provided in Table 2. The computational domain was generated using a 'sphere primitive' centered at the model moment center with a radius of 100c (2400 inches). Differences in surface resolution are apparent in Fig. 1 where a top view of the fuselage and wings are provided for each grid labeled from 'very coarse' to 'very fine'. Also provided in Table 2 are the maximum surface triangle size, $\Delta s_{\text{surface}}$, and the wing leading edge element size, Δs_{LE}, which were reduced systematically by an order of magnitude from the 'very coarse' to 'very fine' grids. The trailing edge resolution for the very coarse grid is similar to what is used in panel method or a lower fidelity Euler solver. The grid refinement factor, r, for each successive Euler grid is provided in Table 2 and defined by[24]

$$r = (N_1/N_2)^{1/d} \tag{1}$$

where N_1 and N_2 are the number of cells or nodes in the finer and coarser grids being compared and d is the spatial dimension (3 for these grids). Because Kestrel is a cell-centered solver, the cell count is used in the refinement factor calculations provided in Table 2. However, the refinement factors provided in Table 2 indicate that the volume spatial resolution was not increased by a large amount outside of the immediate surface triangulation.

The viscous grids share the same aircraft surface triangulation as the medium Euler grid. The details of the four DDES grids tested are available in Table 3. The viscous layers were generated using the best practices provided by Nichols[25] with an estimated y^+<1 and a geometric growth factor (GF) of 1.2. A Reynolds number of Re_c=2.13×10^6 was assumed for grid generation corresponding to Ma_∞=0.16 at 2500

Table 2. Euler grid node and cell counts along with three-dimensional refinement factor.

Grid	Nodes	Cells	r	$\Delta s_{\text{surface}}$	Δs_{LE}
VC – Very Coarse	0.656×10^6	3.797×10^6	-	4.000 in	0.400 in
C – Coarse	1.083×10^6	6.284×10^6	1.183	2.000 in	0.200 in
M – Medium	2.035×10^6	11.81×10^6	1.234	1.000 in	0.100 in
F – Fine	3.069×10^6	17.84×10^6	1.147	0.750 in	0.075 in
VF – Very Fine	5.432×10^6	31.61×10^6	1.210	0.500 in	0.050 in

ft. The geometric growth function to calculate the the i^{th} cell thickness is given as

$$\Delta s_i = \Delta s_1 (GF)^{i-1} \tag{2}$$

and the total height of the boundary-layer grid constructed with n layers is calculated via summation

$$\delta_H = \sum_{i=1}^{n} \Delta s_1 (GF)^{i-1}. \tag{3}$$

The turbulent boundary layer thickness, $\delta_{99\%}$, estimated with flat plate theory[26] at this Re_c is approximately $\delta_{99\%} \approx 0.5$ in. The initial wall-normal grid spacing, Δs_1, was also estimated using turbulent flat plate theory to be $\Delta s_1 = 2.75\times10^{-4}$ in. The number of layers for each of the grids detailed in Table 3 were chosen so that the total viscous grid height would be $\delta_H \approx 2\times\delta_{99\%}$ or 1 inch. A viscous grid containing the landing gear was also created at the medium boundary layer resolution, denoted $\text{M}^{\text{Gear}}_{\text{MBL}}$. The addition of the landing gear geometry increased the cell count by approximately 62%, i.e., $\text{M}^{\text{Gear}}_{\text{MBL}}/\text{M}_{\text{MBL}} \approx 1.62$.

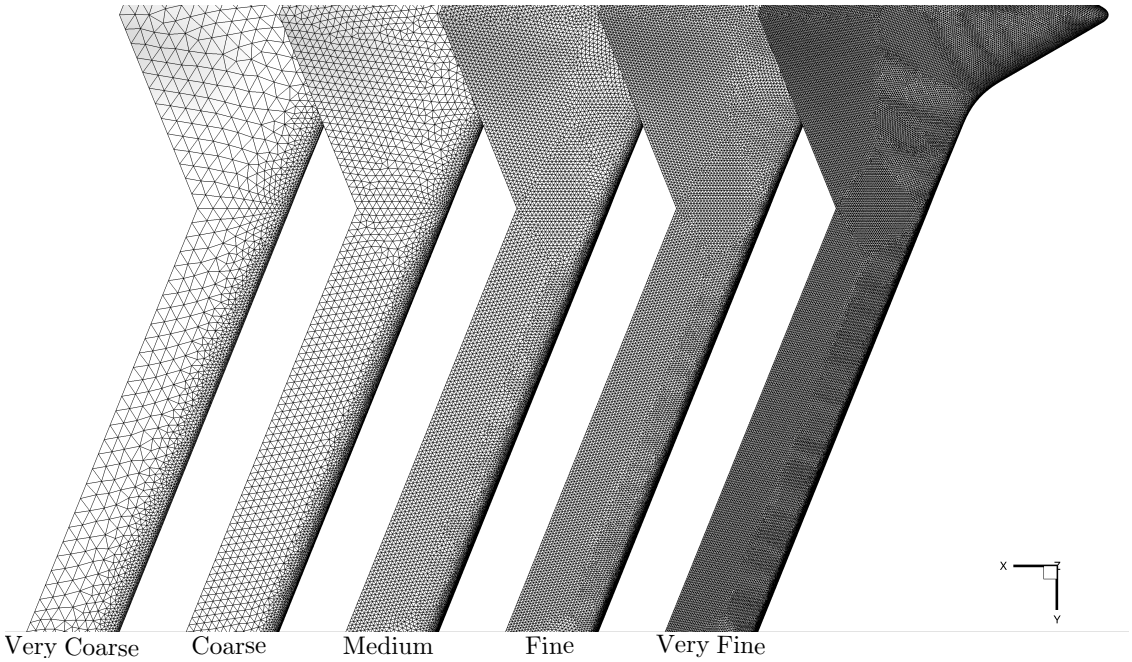

Figure 1. X-56A semispan surface triangulation comparisons for the five resolutions investigated.

Table 3. DDES grid node and cell counts. These grids all share the medium Euler surface triangulation and only differ in initial wall-normal spacing and stretching ratio.

Grid	Nodes	Cells	r	Δs_1	GF	n	δ_H
M_{CBL} – Coarse BL	4.580×10^6	13.928×10^6	–	3.670×10^{-4} in	1.2	35	1.08 in
M_{MBL} – Medium BL	4.676×10^6	14.161×10^6	1.006	2.750×10^{-4} in	1.2	36	0.973 in
M_{FBL} – Fine BL	4.918×10^6	14.635×10^6	1.011	1.830×10^{-4} in	1.2	48	0.964 in
$\text{M}^{\text{Gear}}_{\text{MBL}}$ – Medium BL with Gear	6.866×10^6	22.950×10^6	-	2.750×10^{-4} in	1.2	36	0.973 in

Figure 2(a) shows a cut plane of the volume mesh for half of the vehicle cutting through wing at approximately $0.5c$. A detailed view of the boundary layer grid, composed of prisms is provided in Fig. 2(b). This figure illustrates that the boundary layer grid is grown to a significant height. This was done to ensure high quality elements near the surface and to accommodate separated flow as the wing twists and deforms during an aeroelastic simulation. Figure 2(c) shows an x and y cut-plane through the landing gear to illustrate the prism layer growth near the intersections of the small-scale components.

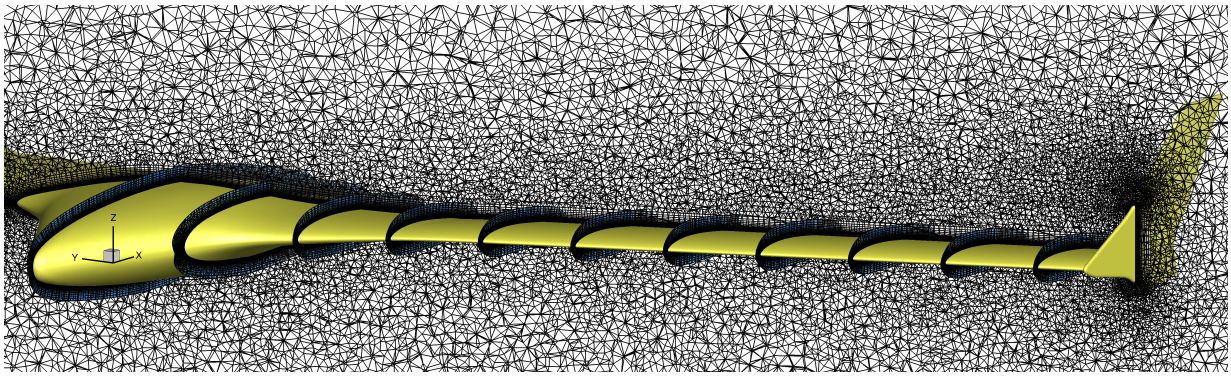

(a) semispan view

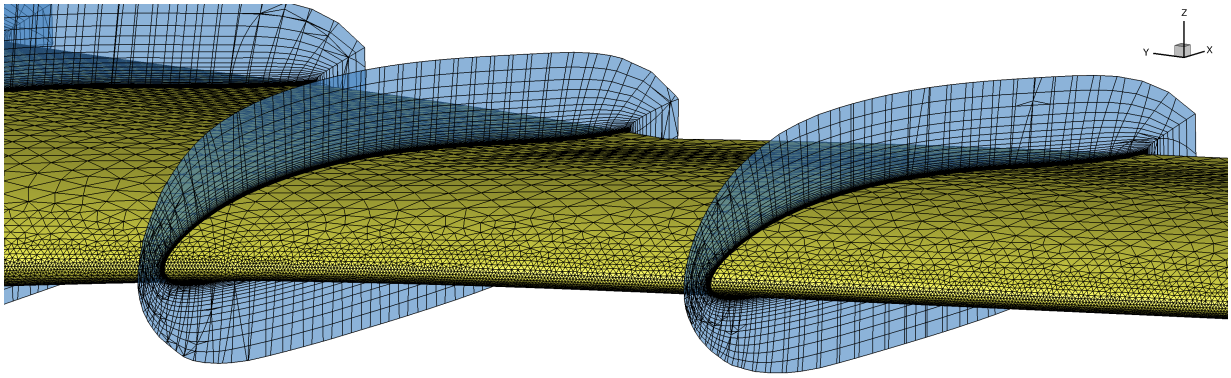

(b) detailed view of prism layers

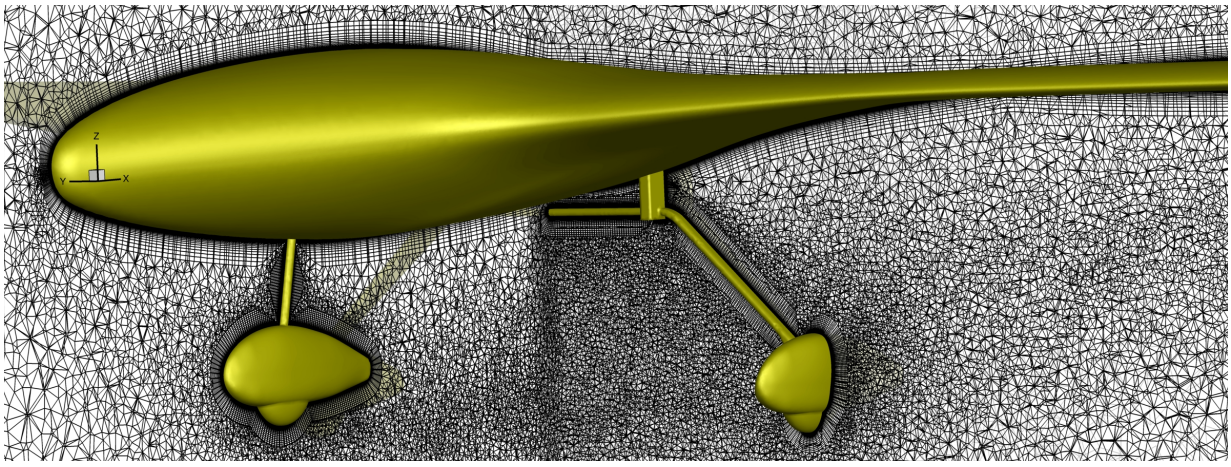

(c) detailed view of landing gear region

Figure 2. Volume grid cut-planes of the M_{MBL} grids.

III.C. Structural Model

The structural model that forms the basis of this work was originally developed at Lockheed Martin Skunkworks and further validated and calibrated to match ground vibration test results from NASA Armstrong.[10,27] It is a finite element (FE) model constructed in NASTRAN containing 8249 nodes. A lower fidelity modal model is used in this work instead of the full FEM NASTRAN model. The full modal solution contains 6 rigid-body modes and 34 elastic modes with a range from 3-60 Hz where numerous modes contain control surface displacements.

The structural model and modal solution was read by PyNastran[28] and written into standard `F06` and `BDF` formats for Kestrel. PyNastran is an application program interface (API) to the legacy formats used by NASTRAN that allows users to write Python code to read data from the numerous NASTRAN formats. Kestrel is then used to convert the `BDF` and `F06` files into a single `CSD` file. Modifications to the `F06` file included the addition of `EIGR` or `EIGRL` NASTRAN card entries so the Kestrel reader functions parsed the modal solution correctly. The mode shapes were visualized using a responding structure simulation without invoking the KCFD solver. Furthermore, specific mode shapes were omitted during a simulation by listing only those of interest in the Kestrel input file. In this work, four elastic modes corresponding to symmetric first wing bending (S1WB), anti-symmetric first wing bending (A1WB), symmetric first wing torsion (S1WT), and anti-symmetric first wing torsion (A1WT) modes were the only elastic modes considered; they were shown by Pak and Truong[10] to be the most critical to predicting the three flutter modes of the X-56A flexible wing design.

Kestrel uses a tolerance in the modal structure file to specify where nodes too close together can be eliminated, thus reducing the size of the mapping from the fluid surface mesh to the full list of structural nodes. The structural mode shapes are then mapped to the fluid surface mesh during the simulation initialization. In this work, the tolerance specified in the Kestrel `CSD` file was 3.5 inches. A visualization of the structural nodes that remain after this filtering process is provided in Fig. 3.

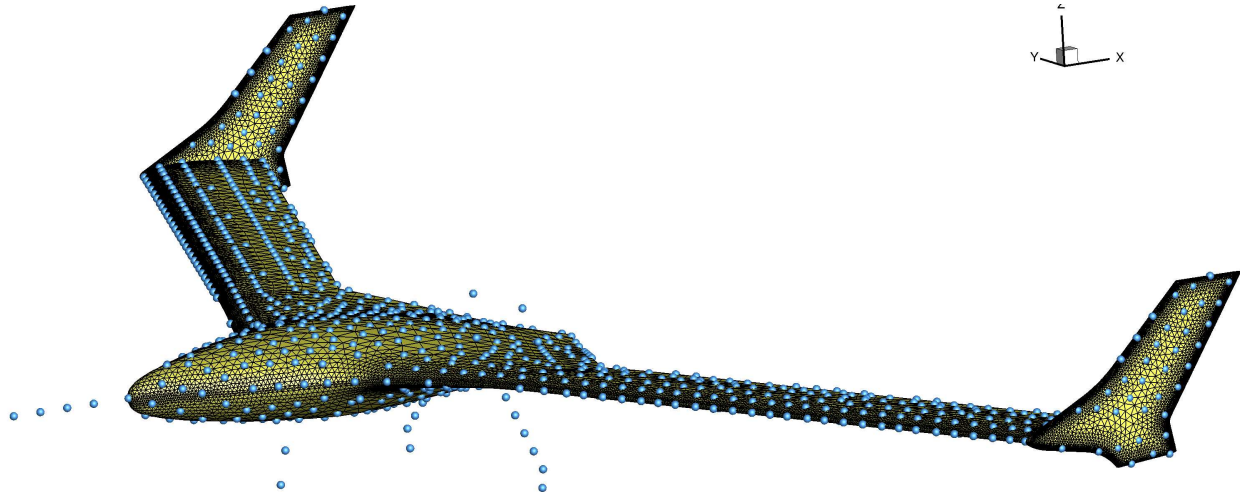

Figure 3. Fluid mesh surface triangulation with filtered structural nodes.

Kestrel output provides the generalized modal weights and generalized modal loads. However, it is advantageous to present which modes are the most active using a quantity that is insensitive to mass or displacement scaling. As a result, the modal effective mass, m_n^{eff} was computed, and is defined by

$$m_n^{\text{eff}}(t) = [\omega_n(t)]^2 m_n \tag{4}$$

where $\omega_n(t)$ is the modal weight for mode n at time t from Kestrel output and m_n is the generalized modal mass for mode n from the Kestrel `CSD` file.

IV. Results

IV.A. Rigid Body Results

Grid Convergence

In order to assess spatial grid requirements necessary for accurate lift and pitching moment calculations a grid independence study was conducted. The grid convergence index (GCI) is a quantity proposed by Roache[29] to more accurately present the uncertainty due to changes in the spatial resolution; it is defined as

$$GCI = \frac{F_s}{r^p - 1}\left|\frac{f_2 - f_1}{f_1}\right| \tag{5}$$

where F_s is a safety factor of 3.0, p is the order of the spatial scheme employed (2.0 assumed here), and f_1, f_2 are the finer and coarser grid global solution quantities being compared, e.g., C_L, C_D or C_M.

The results for the Euler grid GCI calculations are given in Table 4 for Ma_∞=0.15, α=2°, and β=0° for each of the time-averaged aerodynamic coefficients. Each simulation begins with 1000 start-up iterations to improve convergence behavior. Each coefficient used in the GCI calculations was averaged over the final 1.0 second (2000 time steps) of physical time using a time step of Δt=5×10^{-4} seconds.

Table 4. Grid convergence index, GCI, calculations for the Euler grids employed at Ma_∞=0.15, α=2°, and β=0°.

Grid	r	GCI_{CL}	GCI_{CD}	GCI_{CM}
VC	–	–	–	–
C	1.183	40.80%	189.9%	119.0%
M	1.234	13.78%	210.3%	34.97%
F	1.147	12.52%	69.51%	31.36%
VF	1.210	9.491%	26.35%	23.42%

A GCI study was also performed for the viscous grids that were refined in the wall-normal direction within the boundary layer. The results for this study at Ma_∞= 0.15, α=2°, β=0° are given in Table 5. The results presented are time averaged over the final 1.0 second (2000 time steps) also using a time step of Δt=5×10^{-4} seconds. The GCI values for this study are relatively large due to the extremely small value of r since the viscous grids differ only in boundary-layer grid construction parameters. The observed max(y^+) values reported by Kestrel are within the required grid spacing[25] for accurate skin friction drag predictions.

Table 5. Grid convergence index, GCI, calculations for the viscous grids employed at Ma_∞=0.15, α=2°, and β=0°. Note all grids have the same surface triangulation based on the medium resolution Euler grid.

Grid	r	GCI_{CL}	GCI_{CD}	GCI_{CM}	max(y^+)
M_{CBL}	–	–	–	–	0.647
M_{MBL}	1.006	155.3%	70.30%	571.1%	0.508
M_{FBL}	1.011	19.62%	19.95%	59.62%	0.388

Angle of Attack Sweep

Aerodynamic coefficients from rigid-wing X-56A flight tests, Lockheed Martin wind tunnel tests, and Kestrel CFD results are presented in Fig. 4. The medium resolution Euler grid labeled 'M' in Table 2 and the viscous grid labeled 'M_{MBL}' in Table 3 are used in this comparison. Each CFD aerodynamic coefficient result is post-processed from an unsteady KCFD simulation time averaged over the final 1.0 second (2000 time steps) using a time step of Δt=5×10^{-4} seconds. In Fig. 4(a) the total lift coefficient, C_L, is plotted against angle-of-attack, α. The wind tunnel and flight test results are in very good agreement, but the CFD results over-predict C_L at the higher α values. In Fig. 4(b) C_L is plotted against the total drag coefficient, C_D, where it is shown that flight test predicts the highest drag. The Kestrel results under-predict the wind tunnel C_D by a significant margin if the landing gear is not included. However, the SA-DDES results with the landing gear included match the wind tunnel results very well. Figure 4(c) plots the pitching moment, C_M, against C_L and illustrates that the Kestrel results over predict the wind tunnel findings, but neither the wind tunnel nor the CFD accurately matched the pitching moment from flight test.

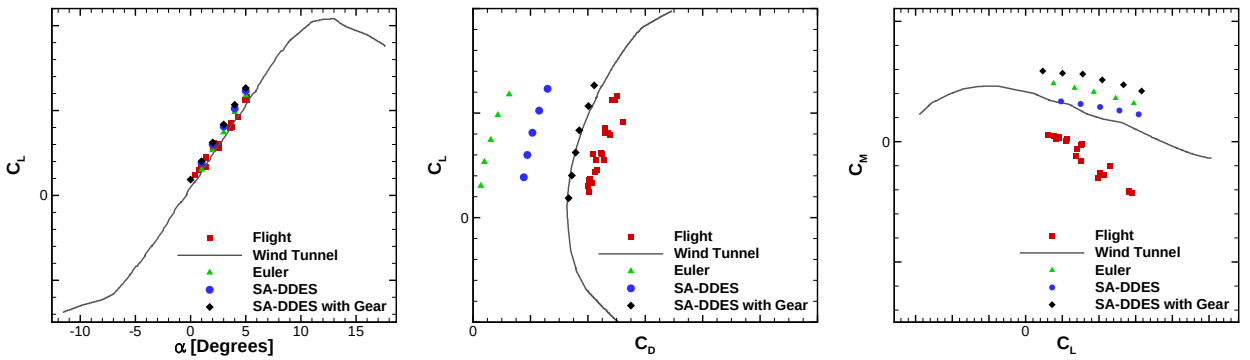

(a) C_L vs. α (b) C_L vs. C_D (c) C_M vs. C_L

Figure 4. Aerodynamic coefficients plotted for the rigid wing aircraft with flight test and wind tunnel data. Inviscid (Euler) and viscous (SA-DDES) results are included for the baseline CFD (without landing gear) and viscous (SA-DDES) results are included for the grid with the landing gear.

IV.B. Aeroelastic Simulation Results

Aeroelastic simulation predictions are provided in Fig. 5 utilizing the $\mathrm{M_{MBL}}$ and $\mathrm{M^{Gear}_{MBL}}$ grids and the four, previously mentioned, primary elastic modes. The time step was identical for both simulations, Δt=5×10^{-4} seconds. The user-defined ramp-and-hold maneuver is provided in Fig. 5(a) with the freestream conditions of Ma_∞=0.12, α=1°, and β=0°. The grid is translated at different acceleration values to obtain the discrete Ma_∞ number plateaus using a Kestrel `motion` file. A hold is performed at every ΔMa_∞=0.02 up to a maximum of Ma_∞=0.24. Due to the low frequency nature of body-freedom flutter, each constant Ma_∞ plateau in the maneuver is held for at least 3 periods of the lowest frequency elastic mode included. These aeroelastic simulations were run for 30τ where $\tau = tf_{\mathrm{S1WB}}$, t is time, and f_{S1WB} is the frequency of the symmetric first wing bending mode, i.e., the lowest frequency elastic mode. Each simulation consumed approximately 35,000 CPU-core hours using 20 nodes of the Lightning supercomputer (Cray XC30, 24 cores/node, Intel Xeon E5-2697v2 2.7 GHz) at the AFRL DoD Supercomputing Resource Center.

The time history of C_L, C_D, and C_M is provided in Fig. 5(b-d) respectively. The onset of a low-frequency flutter mode occurs when the aircraft is at Ma_∞=0.20 at τ≈19.8 and is exacerbated when the maneuver accelerates toward Ma_∞=0.22 at τ≈21.3. This flutter mode is at a frequency of f_{SBFF}≈0.45f_{S1WB} which is a reasonable estimate based on previous investigations[10] where it was found to be 0.66f_{S1WB} using potential flow aerodynamics at Ma_∞=0.14 conditions. The time histories of the aerodynamic coefficients are very similar for the two configurations, but larger C_D and C_M values are observed for the grid with the landing gear. Kestrel simulations utilizing the landing gear grid remained stable for a longer time history. This was surprising due to the additional smaller-scale geometric elements, but the deformation in that area is not as exaggerated as that seen at the outboard locations.

Figure 6 provides a detailed view of C_L for τ=20-30 after flutter onset along with an illustration of the deformed vehicle shape (unmagnified) at peak locations. This figure illustrates that at flutter onset, the vehicle is experiencing wingtip deflections on the order of a few percent of span. Once the oscillations begin to grow (peaks E-I), the peak-to-peak wing-tip deflections are on the order of half span are observed. At onset, the lower peaks correspond to washed-in wing-tip deflections. As the lower peaks in C_L approach zero (peak F), the wash-in is reduced and the deflections are downward (peak H). While Kestrel is robust enough to accommodate mesh deformation of these large magnitudes, the displacements would often be considered out of the linear regime where a modal structural model is valid. A nonlinear finite element structure model is required to more accurately model deflection amplitudes of this magnitude.

Figures 7 and 8 illustrate that the two most active modes are symmetric first wing bending (S1WB) and symmetric first wing torsion (S1WT). Therefore, this is the symmetric-body-freedom flutter mode expected from the previous analysis.[10] Based on the deformations visualized in Fig. 6, it is clear that most of the deformation is S1WB, with the S1WT contributing to the wash-in motion at the wingtip. The modal effective mass of the anti-symmetric modes are very small in comparison with S1WB. Overall, the body-freedom flutter observed in these simulations is comprised of approximately 99% S1WB and 1% S1WT.

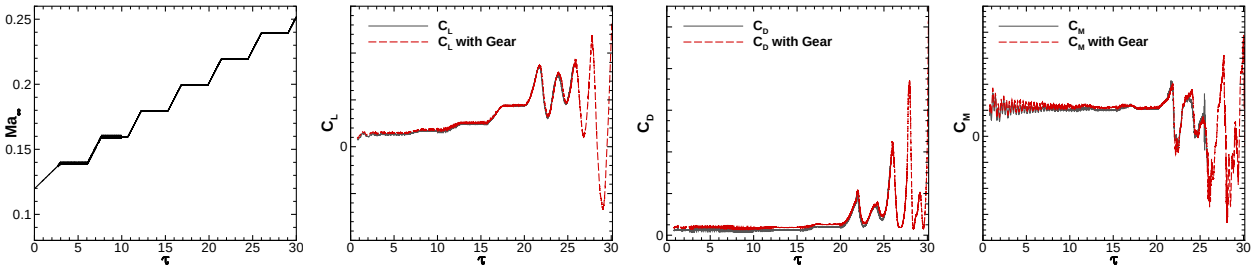

(a) $Ma_\infty(\tau)$ (b) $C_L(\tau)$ (c) $C_D(\tau)$ (d) $C_M(\tau)$

Figure 5. Aerodynamic coefficients plotted against τ for aeroelastic ramp and hold maneuver at α=1°, an altitude of 2500 ft, and several Ma_∞ values for with and without the landing gear..

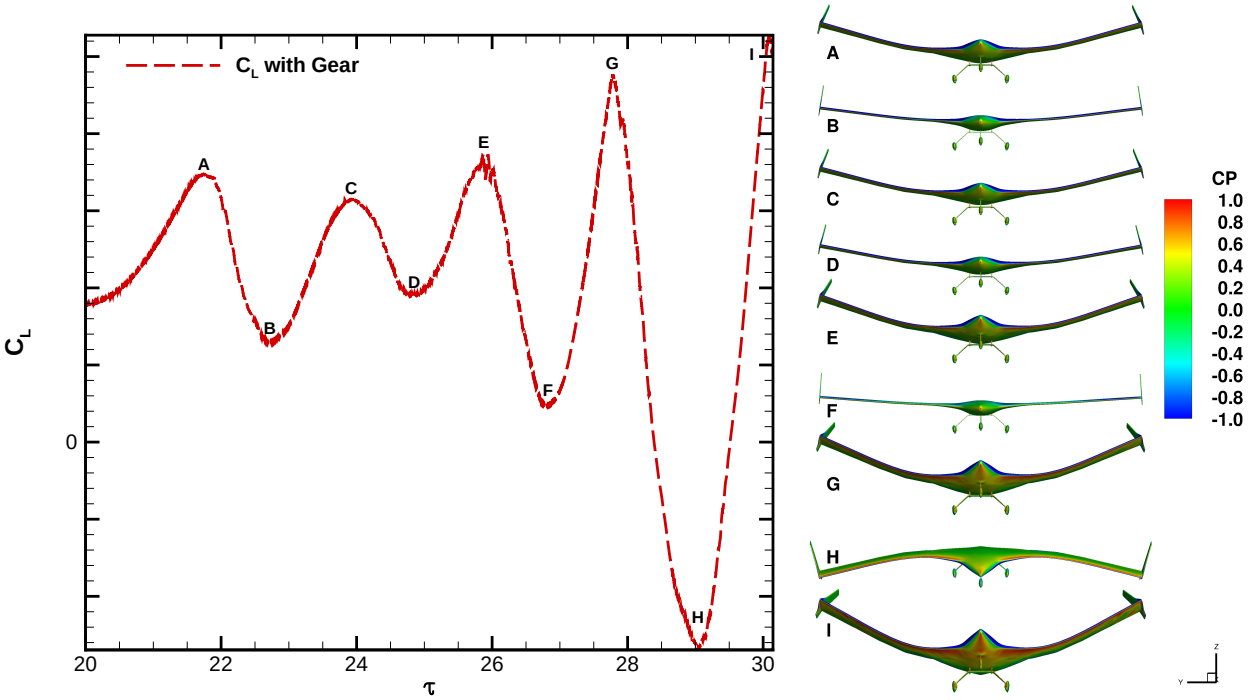

(a) $C_L(\tau)$ (b) C_p contours

Figure 6. Lift coefficient, C_L, plotted versus τ for aeroelastic ramp and hold maneuver at α=1°, an altitude of 2500 ft, and several Ma_∞ values with the landing gear post flutter onset. Peak values are labeled, and corresponding predicted non-amplified vehicle deformation colored by coefficient of pressure, C_p.

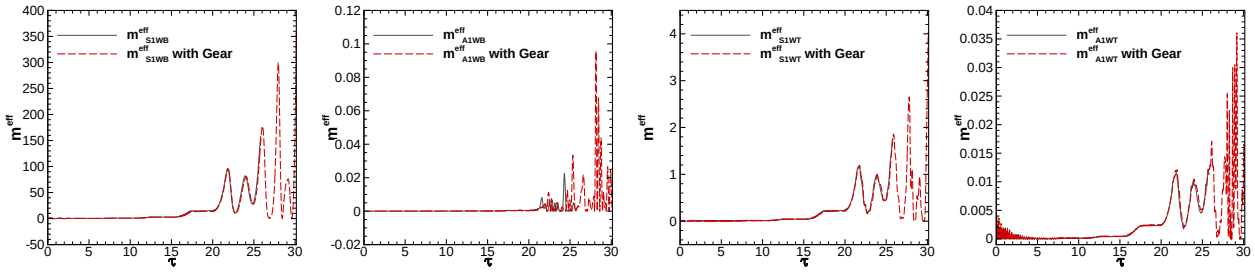

(a) $m^{\text{eff}}_{\text{S1WB}}(\tau)$ (b) $m^{\text{eff}}_{\text{A1WB}}(\tau)$ (c) $m^{\text{eff}}_{\text{S1WT}}(\tau)$ (d) $m^{\text{eff}}_{\text{A1WT}}(\tau)$

Figure 7. Effective modal mass, M_{eff}, plotted versus τ for aeroelastic ramp and hold maneuver at α=1°, an altitude of 2500 ft, and several Ma_∞ values for grids with and without the landing gear.

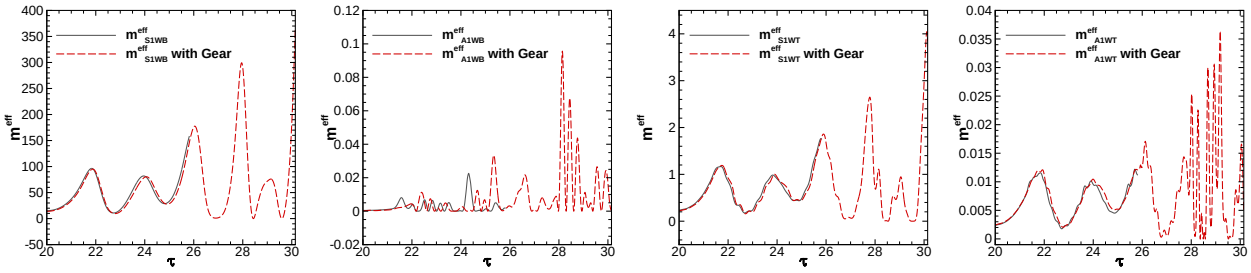

(a) $m^{\text{eff}}_{\text{S1WB}}(\tau)$ (b) $m^{\text{eff}}_{\text{A1WB}}(\tau)$ (c) $m^{\text{eff}}_{\text{S1WT}}(\tau)$ (d) $m^{\text{eff}}_{\text{A1WT}}(\tau)$

Figure 8. Post flutter onset effective modal mass, M_{eff}, plotted versus τ from aeroelastic simulations utilizing ramp and hold maneuver at α=1°, an altitude of 2500 ft, and several Ma_∞ values for grids with and without the landing gear.

V. Conclusions

This work discusses the use of the U.S. Department of Defense CREATE$^{\text{TM}}$-AV tools for simulating body-freedom-flutter of the X-56A using a high-fidelity time-domain approach. The geometry of the X-56A needed to be repaired and made 'water-tight' in an outside CAD package prior to use in Capstone. Capstone was able to generate valid grids for inviscid and turbulent viscous computations utilizing models with and without landing gear components. The translation of the validated NASTRAN structural modes into the Kestrel `CSD` format required little modification and could be performed via the Kestrel user interface or core Python. With appropriate grid deformation settings in Kestrel, the symmetric body-freedom flutter onset Mach number was predicted in the time-domain at constant altitude and constant angle-of-attack by performing a ramp-and-hold maneuver. Each aeroelastic maneuver was computed on the AFRL DSRC Lightning supercomputer in approximately 3 days on 480 CPU-cores. Follow-on validation studies using these inputs are welcome after flexible-wing flight tests are completed.

Acknowledgments

The authors thank the CREATE$^{\text{TM}}$STAR Program and Pete Flick of the Air Force Research Laboratory for their generous support and the CREATE$^{\text{TM}}$-AV developers of Capstone and Kestrel for their efforts. This work could not have been completed without the assistance of the CREATE$^{\text{TM}}$Quality Assurance Team, specifically, Benjamin Hallissy, David Hine, and Theresa Shafer. The authors are grateful to the NAVY DSRC for use of Haise, AFRL DSRC for the use of Lightning, and Joseph Laiosa for his assistance in providing access to HPC resources. The authors would also like to express our gratitude for the support of Chan-Gi Pak and Wesley Li of NASA Armstrong Flight Research Center, Donald Malloy and SMART Scholar Dalton Baier of the Arnold Engineering Development Complex (the latter for writing the modal effective mass post-processing scripts), and Crystal Pasiliao of the AFRL Munitions Directorate.

References

[1]Love, M. H., Zink, P. S., Wieselmann, P. A., and Youngren, H., "Body Freedom Flutter of High Aspect Ratio Flying Wings," *AIAA Paper 2005-1947*, 2005, pp. 1–23.

[2]Beranek, J., Nicolai, L., Buonanno, M., Burnett, E., Atkinson, C., Holm-Hansen, B., and Flick, P., "Conceptual Design of a Multi-utility Aeroelastic Demonstrator," *AIAA Paper 2010-9350*, 2010, pp. 1–15.

[3]Pendleton, E. W., Bessette, D., Field, P. B., Miller, G. D., and Griffin, K. E., "Active Aeroelastic Wing Flight Research Program: Technical Program and Model Analytical Development," *Journal of Aircraft*, Vol. 37, No. 4, 2000, pp. 554–561.

[4]Suh, P. M. and Mavris, D. N., "Modal Filtering for Control of Flexible Aircraft," *AIAA Paper 2013-1741*, 2013, pp. 1–38.

[5]Suh, P. M., Chin, A. W., and Mavris, D. N., "Robust Modal Filtering and Control fo the X-56A Model with Simulated Fiber Optic Sensor Failures," *AIAA Paper 2014-2053*, 2014, pp. 1–27.

[6]Suh, P. M., Chin, A. W., and Mavris, D. N., "Virtual Deformation Control of the X-56A Model with Simulated Fiber Optic Sensors," *AIAA Paper 2013-4844*, 2013, pp. 1–32.

[7]Mangalam, S. M. and Brenner, M. J., "Fly-by-Feel Sensing and Control: Aeroservoelasticity," *AIAA Paper 2014-2189*, 2014, pp. 1–8.

[8]Li, W. W. and Pak, C.-G., "Mass Balancing Optimization Study to Reduce Flutter Speeds of the X-56A Aircraft," *Journal of Aircraft*, 2014, pp. 1–21.

[9]Li, W. W. and Pak, C.-G., "Aeroelastic Optimization Study Based on the X-56A Model," *AIAA Paper 2014-2052*, 2014, pp. 1–21.

[10]Pak, C.-G. and Truong, S., "Creating a Test Validated Finite-Element Model of the X-56A Aircraft Structure," *Journal of Aircraft*, Vol. 52, No. 5, 2015, pp. 1644–1667.

[11]Nicolai, L., Hunten, K., Zink, S., and Flick, P., "System Benefits of Active Flutter Suppression for a SensorCraft-Type Vehicle," *AIAA Paper 2010-9349*, 2010, pp. 1–12.

[12]Edwards, J. W., "Unsteady Aerodynamic Modeling and Active Aeroelastic Control," Tech. Rep. NASA-CR-148019, Stanford University Center for Systems Research, 1978.

[13]Miller, G. D., Wykes, J. H., and Brosnan, M. J., "Rigid-body structural mode coupling on a forward swept wing aircraft," *Journal of Aircraft*, Vol. 20, No. 8, 1983, pp. 696–702.

[14]Morton, S. A., McDaniel, D. R., Sears, D. R., Tillman, B., and Tuckey, T. R., "Kestrel – A Fixed-Wing Virtual Aircraft Product of the CREATE Program," *AIAA Paper 2009-0338*, 2009, pp. 1–15.

[15]Morton, S. A., Lamberson, S. E., and McDaniel, D. R., "Static and Dynamic Aeroelastic Simulations using Kestrel – A CREATE Aircraft Simulation Tool," *AIAA Paper 2012-1800*, 2009, pp. 1–16.

[16]McDaniel, D. R. and Tuckey, T. R., "Multiple Bodies, Motion, and Mash-Ups: Handling Complex Use-Cases with Kestrel," *AIAA Paper 2014-0415*, 2014, pp. 1–21.

[17]Lamberson, S. E. and Hallissy, B. P., "Aeroelastic Simulations with Modal and Finite-Element Structural Solvers Using HPCMP CREATE^{TM}-AV Kestrel," *AIAA Paper 2014-0041*, 2014, pp. 1–25.

[18]Spalart, P. R. and Allmaras, S. R., "A One-Equation Turbulence Model for Aerodynamic Flows," *AIAA Paper 92-0439*, 1992, pp. 1–22.

[19]Spalart, P. R., Deck, S., Shur, M. L., Squires, K. D., Strelets, M. K., and Travin, A., "A new version of detached-eddy simulation, resistant to ambiguous grid densities," *Theoretical and Computational Fluid Dynamics*, Vol. 20, No. 3, 2006, pp. 181–195.

[20]Barth, T. J. and Jespersen, D. C., "The Design and Application of Upwind Schemes on Unstructured Meshes," *AIAA Paper 89-0366*, 1989, pp. 1–12.

[21]vanLeer, B., Thomas, J. L., Roe, P. L., and Newsome, R. W., "A Comparison of Numerical Flux Formulas for the Euler and Navier–Stokes Equations," *AIAA Paper 87-1104*, 1987, pp. 1–6.

[22]Thomas, J. L., vanLeer, B., and Walters, R. W., "Implicit Flux-Split Schemes for the Euler Equations," *AIAA Journal*, Vol. 28, No. 2, 1990, pp. 973–974.

[23]Eymann, T. A., Nichols, R. H., McDaniel, D. R., and Tuckey, T. R., "Cartesian Adaptive Mesh Refinement with the HPCMP CREATE^{TM}-AV Kestrel Solver," *AIAA Paper 2015-0040*, 2015, pp. 1–20.

[24]Oberkampf, W. L. and Roy, C. J., *Verification and Validation in Scientfic Computing*, Cambridge, 2010.

[25]Nichols, R. H., "Turbulence Models and Their Application to Complex Flows," Tech. rep., University of Alabama Birmingham, 2010, Version 4.01.

[26]White, F. M., *Viscous Fluid Flows*, McGraw–Hill, 2nd ed., 1991.

[27]Pak, C.-G. and Truong, S., "Creating a Test Validated Structural Dynamic Finite Element Model of the X-56A Aircraft," *AIAA Paper 2014-3157*, 2014, pp. 1–39.

[28]Doyle, S. and Danial, A., "PyNastran: A Python-based interface tool for Nastran's file formats," 2014, User Manual, Release 0.6.0, https://github.com/SteveDoyle2/pynastran.

[29]Roache, P. J., "Perspective: a method for uniform reporting of grid refinement studies," *Journal of Fluids Engineering*, Vol. 116, 1994, pp. 405–413.